

Alma Mater Studiorum Università di Bologna  
Archivio istituzionale della ricerca

Analysis of the effects of shading screens on the microclimate of greenhouses and glass facade buildings

This is the final peer-reviewed author's accepted manuscript (postprint) of the following publication:

*Published Version:*

Santolini, E. (2022). Analysis of the effects of shading screens on the microclimate of greenhouses and glass facade buildings. BUILDING AND ENVIRONMENT, 211(1 March 2022), 1-18 [10.1016/j.buildenv.2021.108691].

*Availability:*

This version is available at: <https://hdl.handle.net/11585/895329> since: 2024-01-29

*Published:*

DOI: <http://doi.org/10.1016/j.buildenv.2021.108691>

*Terms of use:*

Some rights reserved. The terms and conditions for the reuse of this version of the manuscript are specified in the publishing policy. For all terms of use and more information see the publisher's website.

This item was downloaded from IRIS Università di Bologna (<https://cris.unibo.it/>).  
When citing, please refer to the published version.

(Article begins on next page)

See discussions, stats, and author profiles for this publication at: <https://www.researchgate.net/publication/357585616>

# Analysis of the effects of shading screens on the microclimate of greenhouses and glass facade buildings

Article in *Building and Environment* · January 2022

DOI: 10.1016/j.buildenv.2021.108691

CITATIONS

19

6 authors, including:



**Enrica Santolini**

University of Bologna

35 PUBLICATIONS 304 CITATIONS

[SEE PROFILE](#)



**Marco Bovo**

University of Bologna

79 PUBLICATIONS 779 CITATIONS

[SEE PROFILE](#)

READS

149



**Paolo Guidorzi**

University of Bologna

48 PUBLICATIONS 342 CITATIONS

[SEE PROFILE](#)



**Patrizia Tassinari**

University of Bologna

142 PUBLICATIONS 1,607 CITATIONS

[SEE PROFILE](#)

# Analysis of the shading screen effects on greenhouse environmental conditions evaluated with CFD simulations

Enrica Santolini<sup>a</sup>, Beatrice Pulvirenti<sup>b</sup>, Paolo Guidorzi<sup>b</sup>, Marco Bovo<sup>a</sup>,  
Daniele Torreggiani<sup>a</sup>, Patrizia Tassinari<sup>a</sup>

<sup>a</sup>*Department of Agricultural and Food Sciences, University of Bologna, Via Giuseppe Fanin 48, 40127, Bologna, Italy*

<sup>b</sup>*Department of Industrial Engineering, University of Bologna, via Terracini 34, 40131, Bologna, Italy*

---

## Abstract

Shading devices are widely used in the protected crop cultivation, mostly in the Mediterranean area, since they allow to reduce the strong solar radiation effects in the closed environment. On the contrary, they have negative effects on the ventilation efficiency of the greenhouse especially if they have low porous texture and therefore they represent an obstacle to passage of air. Moreover, investigations about indoor environmental conditions and distributions can allow to improve the management of indoor climate, by means of the optimization of greenhouse structure and air conditioning systems. This requires the characterization and the modeling of the processes involved, and in particular of the convective heat transfer. In recent years, Computational Fluid Dynamics (CFD) methods have been employed to investigate scalar and vector variables which determines greenhouse microclimate with respect to its structural specifications and equipment. So far, the majority of studies, related to the effects of shade screens on greenhouse climate, focused on experimental investigation based on analytic model. Only few studies have used CFD simulations to explore the response of greenhouse climate factors to the change of shading parameters. The present study aims to investigate, by means of a CFD approach, the distribution of temperature and air flow in a naturally ventilated three-span glass greenhouse, taking into consideration the external incident radiation, the optical properties of the materials and the presence of shading devices inside the structure.

Corresponding Author: enrica.santolini2@unibo.it

**Keywords:** Natural Ventilation, Solar radiation, CFD Modeling, Greenhouse, Shading screens

---

## 1. Introduction

The Computational Fluid Dynamics (CFD) analyses are nowadays a powerful tool for modeling air flows and climate patterns in agricultural structures, like greenhouses. The CFD allows to investigate the influence of the

---

<sup>1</sup>DOI: 10.1016/j.buildenv.2021.108691.

36 greenhouse design parameters, wind direction, location of the mechanical ven-  
37 tilation devices, on different microclimatic parameters like temperature and  
38 humidity distributions, ventilation flow rate and incident solar radiation (Roy  
39 and Boulard, 2005). The use of CFD has been consolidated as a method for  
40 predicting also the climate conditions of inner crops by resolving the equations  
41 of heat and mass transfer for an accurate mesh of discrete locations (Boulard  
42 et al., 2002).

43 In Mediterranean countries, a concerning aspect for the crop growth is the in-  
44 door climate management during the hot and sunny days usually characterized  
45 by high-intensity solar radiation (He et al., 2014). The climate management is  
46 a fundamental aspect for a productive greenhouse since it influences not only  
47 the growth of crops, but also the energy needs of the facility (Barbaresi et al.,  
48 2020) and then the profitability and sustainability of the sector. Several meth-  
49 ods can be used for cooling the greenhouse environment in order to establish  
50 more suitable conditions for crop growth. Natural ventilation is usually the  
51 first option due to its low cost and simplicity, but it can be insufficient for  
52 controlling heat gain and high temperature peaks during sunny summer days  
53 (Baille, 1999). Then, other cooling methods have to be considered in combi-  
54 nation with natural ventilation (Katsoulas et al., 2001). A solution used more  
55 and more is the introduction of shade screens, which could be placed inter-  
56 nally or externally to the cladding, to attenuate the incoming solar radiation  
57 and to avoid the direct damage of the intense sunshine to the crop’s growth  
58 during hot days (He et al., 2014). In fact, shading can be accomplished in  
59 different ways. A popular technique consists in placing a porous screen over  
60 the cover, adhering to it, or fixed atop the greenhouse, letting the outside air  
61 flow beneath the screen and above the greenhouse (Piscia et al., 2012). These  
62 devices have been investigated under several aspects by the researchers. The  
63 first aspect of interest concerns the evaluation of the effects of the modifica-  
64 tion of some shading parameters (e.g. shade combination, rate and level) on  
65 the air temperature, climate heterogeneity, spectral distribution and growth  
66 of the crops inside the greenhouse (Montero et al., 2013; Piscia et al., 2012;  
67 Kittas et al., 2012; Kittas et al., 2003; Sapounas et al., 2010). On the other  
68 hand, the interest has been focused on the physical properties of the shading  
69 materials (Santolini et al., 2019; Miguel et al., 1997; Miguel, 1998; Miguel and  
70 Silva, 2000; Valera et al., 2006, 2005) and their impact on greenhouse climate  
71 (Santolini et al., 2018; Baxevanou et al., 2010; Kittas et al., 1999).

72 Considering the relevant role of the solar radiation for the plant growth, in-  
73 formation about quantity, quality and spatial distribution of daylight trans-  
74 mitted by greenhouse cladding and shading materials is essential to assess  
75 their influence on growth and development of crops (Baxevanou et al., 2010;  
76 Santolini et al., 2020; Barbaresi et al., 2020). The climate distribution pre-  
77 dictions could allow to save energy and reduce the use of pests, enabling pest  
78 and disease control in a more sustainable way. Moreover, information about  
79 indoor environmental conditions and distributions should help to improve cli-  
80 mate homogeneity, obtained by the optimization of both greenhouse structure

and climate air conditioning systems. This requires the characterization and the modeling of the processes involved, such as convective heat transfer mechanism (Boulard et al., 2002). In recent years, few studies used CFD methods to investigate scalar and vector parameters of the greenhouse microclimate with respect to structural characteristics and conditioning systems (Boulard et al., 2002; Bartzanas et al., 2004; Fatnassi et al., 2006; Santolini et al., 2018). So far, most studies related to the effect of shading screens on greenhouse climate focused on experimental investigations or by adopting analytic models. Few researchers employed numerical methods, e.g. CFD, to explore the response of greenhouse climate by changing the shading parameters. Therefore, the application of CFD approach to investigate the greenhouse microclimate pattern and the shading performances, in different configurations and for the local climate condition, actually is a promising but almost unexplored research field (He et al., 2014).

In the present study, a CFD model has been used to investigate the distributions of both temperature and air flow in a naturally ventilated three-span glass greenhouse, also taking into account the incident solar radiation. The radiative properties of the materials of the envelope and the presence of shading devices have been properly taken into account. In particular, the paper analyses the effects of three shading devices on the indoor conditions of a greenhouse. The three shading devices have similar radiative properties but different textures. Four different environmental scenarios, simulating four different conditions of summer days in the Mediterranean areas, have been analyzed and compared. The study brings together a novel CFD approach and a new method for climate indoor measurements. The novel CFD approach consists in coupling a CFD modeling of radiation and the approach for the simulation of the presence of screens for screens Santolini et al. (2019). The innovative approach for indoor experimental measurements is a patented technique that, by means of acoustic measurements, allows to reach a very accurate determination of the position of the sensors. The innovative method, described and proposed in the present paper, provides very accurate evaluations of the shading effect of the different screens in the analyzed scenarios. This approach allows to increase the knowledge of the screens behavior in protected crop cultivation and provides useful indications about their application in this sector.

## 2. Materials and Methods

The research has been developed by means of both experimental tests and numerical models carried out on a case study. It is a three-span greenhouse of the University of Bologna, sited in Imola, Italy (about 30 km East of Bologna). The different spans are separated by glass walls and are connected through internal doors. The investigations have been focused on the SE span, highlighted in blue, visible in Fig. 1. This span is provided with three benches for experimental crop cultivation has an independent control unit for indoor climate control, managing heating and cooling systems, vent opening, and shading

124 curtains.

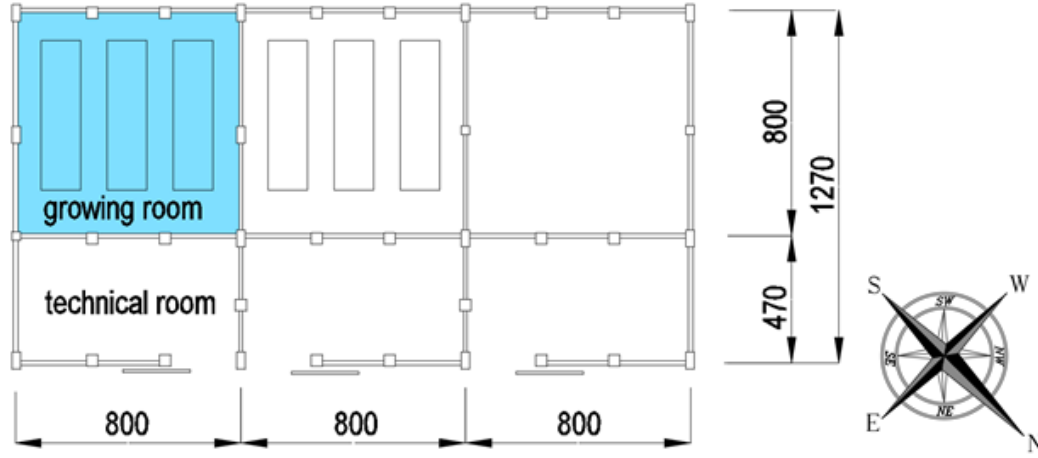


Figure 1: Section in plan of the greenhouse under study.

125 The volume of the span is divided, by means of a wall, in two different  
 126 portions (see Figure 1). The main area is devoted to the cultivation of crops  
 127 whereas the smaller area is a technical room hosting the heating and cooling  
 128 systems. The outcomes of the investigations presented here considers only the  
 129 main area of the span. The numerical simulations have been carried out with  
 130 Ansys-Fluent 17.2 code (Fluent Inc, 2006). The computational domain is a  
 131 parallelepiped with dimensions, in horizontal plane, 244.0 m x 63.5 m and 27.5  
 132 m in the vertical direction.

### 133 2.1. Numerical model description

134 The flow inside the greenhouse is considered unsteady, incompressible and  
 135 turbulent. The flow and the transport phenomena for air flow and the heat  
 136 transfer, are described by the Navier-Stokes equations. The time-averaged  
 137 Navier-Stokes equations, for the mass, momentum and energy transport are  
 138 presented in the following equations (1)(2) (Baxevanou et al., 2010):

$$\frac{\Delta U_i}{\Delta x_i} = 0 \quad (1)$$

$$\rho U_j \frac{\delta U_i}{\delta x_j} = -\frac{\Delta P}{\Delta x_i} + \frac{\delta}{\delta x_j} [(\mu + \mu_t) \frac{\delta U_i}{\delta x_j}] + f_b + S_j \quad (2)$$

139 where  $U$  is the fluid velocity,  $P$  is the fluid pressure,  $\rho$  is the fluid density,  $\mu$   
 140 is the fluid dynamic viscosity,  $\mu_t$  is the turbulent viscosity,  $S_j$  is a source term  
 141 and  $f_b$  is a vector which represents the body forces. The density variation was  
 142 calculated according to the Boussinesq model in order to take into account  
 143 the natural convection effects. The turbulence effects on the flow have been  
 144 implemented in the Re-Normalization Group (RNG) based on  $k-\varepsilon$  model. The  
 145 standard  $k-\varepsilon$  model is a semi-empirical model (see 3 and 4), based on model

146 transport equations for the turbulent kinetic energy ( $k$ ) and its dissipation rate  
147 ( $\varepsilon$ ) (Yakhot et al., 1992).

$$\frac{\delta}{\delta t}(\rho k) + \frac{\delta}{\delta x_i}(\rho k u_i) = \frac{\delta}{\delta x_j}[(\mu + \frac{\mu_t}{\sigma_k}) \frac{\delta k}{\delta x_j}] + G_b + G_k - \rho \epsilon - Y_M + S_k \quad (3)$$

$$\frac{\delta}{\delta t}(\rho \epsilon) + \frac{\delta}{\delta x_i}(\rho \epsilon u_i) = \frac{\delta}{\delta x_j}[(\mu + \frac{\mu_t}{\sigma_\epsilon}) \frac{\delta \epsilon}{\delta x_j}] + C_{1\epsilon} \frac{\epsilon}{k} (G_k + C_{3\epsilon} G_b) - C_{2\epsilon} \rho \frac{\epsilon^2}{k} + S_\epsilon \quad (4)$$

148 The RNG approach, which is a mathematical technique that can be used  
149 to derive a turbulence model similar to the standard  $k$ - $\varepsilon$  model, results in a  
150 modified form of the epsilon equation which attempts to account for the dif-  
151 ferent scales of motion through changes to the generation term. In particular,  
152 the RNG model considers these refinements, visible from the comparison of 3  
153 and 4 with 5 and 6:

$$\frac{\delta}{\delta t}(\rho \epsilon) + \frac{\delta}{\delta x_i}(\rho \epsilon u_i) = \frac{\delta}{\delta x_j}[(\alpha_k \mu_{eff}) \frac{\delta \epsilon}{\delta x_j}] + G_b + G_k - \rho \epsilon - Y_M + S_k \quad (5)$$

$$\frac{\delta}{\delta t}(\rho \epsilon) + \frac{\delta}{\delta x_i}(\rho \epsilon u_i) = \frac{\delta}{\delta x_j}[(\alpha_\epsilon \mu_{eff}) \frac{\delta \epsilon}{\delta x_j}] + C_{1\epsilon} \frac{\epsilon}{k} (G_k + C_{3\epsilon} G_b) - C_{2\epsilon} \rho \frac{\epsilon^2}{k} - R_\epsilon + S_\epsilon \quad (6)$$

- 154 • The RNG model has an additional term in the  $\varepsilon$  equation that signifi-  
155 cantly improves the accuracy for rapidly strained flows;
- 156 • The effect of swirl on turbulence is included in the RNG model, enhancing  
157 accuracy for swirling flows;
- 158 • While the standard  $k$ - $\varepsilon$  model is a high-Reynolds-number model, the  
159 RNG theory provides an analytically-derived differential formula for ef-  
160 fective viscosity that accounts for low-Reynolds-number effects. Effective  
161 use of this feature, however, depends on an appropriate treatment of the  
162 near-wall region.

163 These features make the RNG  $k$ - $\varepsilon$  model more accurate and reliable for a  
164 wider class of turbulent flows. The complete set of the equations can be found  
165 in Lien and Leschziner (1994). The Semi-Implicit Method for Pressure-Linked  
166 Equations (SIMPLE) algorithm has been used to take into account pressure-  
167 velocity coupling and second-order discretization schemes have been used for  
168 convective and viscous terms of the governing equations. The velocity has  
169 been monitored in some particular points of the model in order to assess the  
170 on-grid convergence of the solution. The convergence criteria have been set

171 equal to  $10^{-5}$  for the scaled residuals of each variables.  
 172 For this study, where the radiation plays a significant role, the Discrete Ordi-  
 173 nates Radiation model(DO model) has been used. The model considers both  
 174 the solar radiation and the radiations between the greenhouse surfaces. The  
 175 DO model allows to reach the solution in those applications facing with radia-  
 176 tion on semi-transparent walls and can be applied to both gray and non-gray  
 177 radiation by a gray-band model. The model considers the absorption coeffi-  
 178 cients of the surfaces since they can vary within spectral bands (Raithby, 1999;  
 179 Baxevanou et al., 2010). The DO model solves the general radiation transfer  
 180 equation (RTE) for a set of  $n$  different directions for a finite number of discrete  
 181 solid angles, each one associated with a fixed vector direction. The angles  $\theta$   
 182 and  $\phi$  are the polar and azimuthal angles and they are constants.  
 183 In the simulations, these angles have been divided in four control angle for  $\theta$   
 184 and  $\phi$  (Piscia et al., 2012; Raithby, 1999; Murthy and Mathur, 2008). The ra-  
 185 diation equations were computed every 10 iterations. Baxevanou et al. (2008)  
 186 described in details the DO model applied to CFD models of greenhouses. In  
 187 the model, the specific thermal-radiative characteristics of the materials of the  
 188 greenhouse have been defined, as reported in Tables 1 and 2.

Table 1: Thermal characteristics of the materials, used as initial conditions.

Material	Density ( $\rho$ ) ( $\text{kg m}^{-3}$ )	Conductivity ( $\kappa$ ) ( $\text{W m}^{-1} \text{K}^{-1}$ )	Specific heat capacity ( $C_p$ ) ( $\text{J kg}^{-1} \text{K}^{-1}$ )
Glass	2530	1.2	840
Aluminum	2719	202.4	871
Soil	1620	1.3	1480
Concrete	2200	1.5	1000

Table 2: Radiative characteristics of the materials, used as initial conditions.

Material	Absorbance	Emissivity
Glass	0.7	0.9
Aluminium	0.2	0.5
Soil	0.9	0.925
Concrete	0.6	0.88

189 The walls have been modeled as semi-transparent surfaces of tempered  
 190 glass 4 mm thick, the benches have aluminum structures and surfaces, and the  
 191 pavement has been considered a concrete slab.  
 192 Considering the greenhouse is naturally ventilated, a logarithmic wind profile  
 193 has been set at the inlet of the domain,

$$u_{wind} = \frac{u_*}{\kappa} \log\left(\frac{z + z_0}{z_0}\right) \quad (7)$$



194 from which depends the turbulent kinetic energy ( $k$ ) and the dissipation  
 195 rate ( $\varepsilon$ ):

$$k = \frac{u_*^2}{\sqrt{C_\mu}} \quad (8)$$

$$\varepsilon = \frac{u_*^3}{\kappa(z + z_0)} \quad (9)$$

196 where  $u_*$  is the friction wind speed,  $z$  is the elevation calculated starting  
 197 from the ground level,  $z_0$  is the surface roughness,  $\kappa$  is the von Karman's con-  
 198 stant assumed equal to 0.40 and  $C_\mu$  is a experimental constant. The shading  
 199 devices have been modeled by means of the porous-jump model, based on  
 200 the Darcy-Forchheimer law which relates the pressure drop of the fluid flow  
 201 through a porous medium with its physical characteristics (Santolini et al.,  
 202 2019). Each one of the three screens has been defined by assuming its phys-  
 203 ical and radiative properties, as reported in Table 3 and obtained from the  
 204 experimental tests described in Santolini et al. (2019).

Table 3: Physical and radiative properties of shading devices adopted in the present work.

Screen	Thickness (mm)	Permeability (1/m)	Inertial coefficient (1/m <sup>2</sup> )	$Shading_{dir}$ (%)	$Shading_{diff}$ (%)
H3647	0.36	1.4883	$7.2080 \times 10^{-11}$	43	50
H4215	0.32	0.5794	$2.6627 \times 10^{-09}$	48	53
H5220	0.32	0.2759	$4.9085 \times 10^{-10}$	52	52

205 These screens properties (see Tab.3) depend on the specific grid texture  
 206 which could affect the air distribution, by means of permeability and inertial  
 207 coefficient. In fact, the texture is characterized by a sequence of permeable  
 208 layers, made of a weft of plastic thread, and impermeable layers, made of plastic  
 209 strips. The number and sequence of these two types of strips determines the  
 210 interaction of the screen with the incoming air flow.

## 211 2.2. *Experimental campaign*

### 212 2.2.1. *Data acquisition*

213 An experimental campaign has been conducted during a sunny day (23/04/2018),  
 214 collecting data of direct solar radiation, indoor air velocity and temperature.  
 215 The boundary conditions of the CFD simulations have been defined based on  
 216 these measurements.

217 The solar radiation has been measured by a pyranometer (Delta Ohm with  
 218 accuracy of 10 W/(m<sup>2</sup>)), positioned in the proximity of the greenhouse. The  
 219 averaged direct solar radiation has been calculated as:

$$\frac{1}{n} \sum_{i=0}^n (x_i) \quad (10)$$



Figure 2: Description of the case study greenhouse: (a) Plan view of the building; (b) Inner view of the productive surface; (c) Images of the system used for locating the measurements (yellow circle).

where:  $x_i$  are the single data and  $n$  is the number of measurements. The magnitude and vector components of wind velocity have been collected by a weather station placed *in situ*. The indoor air velocity and temperature have been measured with a hot-wire anemometer (Delta Ohm with accuracy of 0.01 m/s). Each velocity measurement is the average of about 60 data collected in a time period of 2 seconds.

### 2.2.2. Positioning system description

An innovative 3D patented positioning system has been used to define in a precise way the position of the sensors. The system (Guidorzi, Jun 14, 2017) is shown in Fig. 2 (see the yellow circle). It is based on acoustic measurements and is similar, in principle, to the global positioning system (GPS). The components of the system are: a 1 m x 1 m grid with 4 amplified loudspeakers (A, B, C and D in Fig. 3a)), a small microphone, a multi-channel sound card and a computer, running a software created ad-hoc, that manages the measurements and records the acquired data.

The microphone, whose position is to be determined, receives the sounds emitted by the four loudspeakers on the grid. From the four arrival times of the respective acoustic waves and knowing the speed of sound in the air (as a function of the temperature), the 4 distances from the microphone and the loudspeakers are measured. To better understand why it is necessary to measure 4 distances, the problem of determining the position of a point on a 2D plane is considered as example, with reference to Fig. 3b), if only the distance of the unknown position target (yellow point) from a known position point 1 is available, the possible solutions are represented by the black circumference; if the distances of the target from two known position points, 1 and 2, are available, two solutions (intersections of the black and blue circumferences) are possible. Finally, if the distances from three known position points, 1, 2 and 3, are available, a single solution, intersection of the three circumferences,

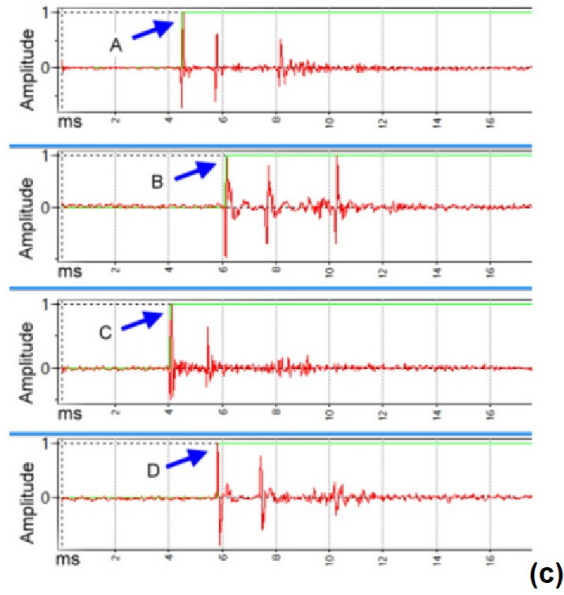
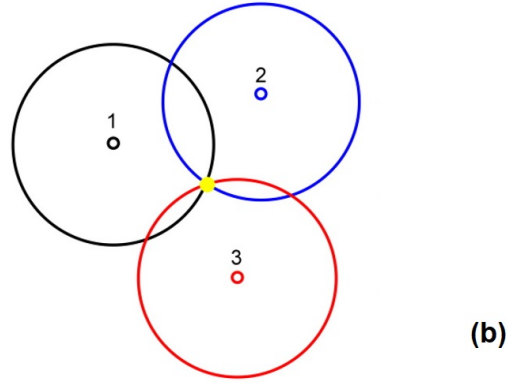
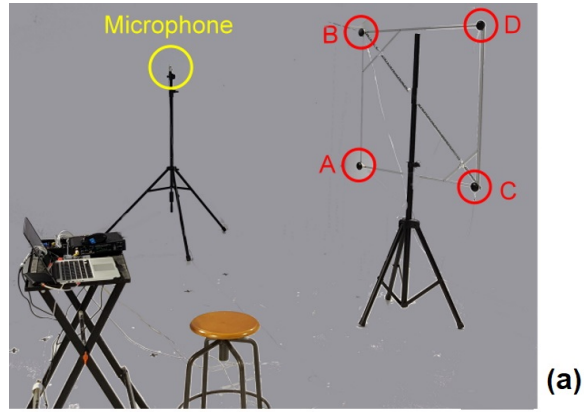


Figure 3: a) Geometrical setup of the 3D positioning system; b) Trilateration on a two-dimensional plane; c) Example of impulse responses acquired by the four loudspeakers.

248 is found. Extending the reasoning to the 3D space, knowing the distance of  
 249 the target point from a point of known position, the possible solutions are on a  
 250 sphere centered in the known position; if the distances from two known points

are available, the possible solutions are on the circumference intersection of the two spheres centered in the known points; if the distances from three known points are available, two possible solutions exist. Finally if the distances from four known points are available, only one solution is obtained and it is the exact position of the target in the 3D space. The intersection point of the four spheres can be found by solving the following system:

$$(x - x_1)^2 + (y - y_1)^2 + (z - z_1)^2 = r_1^2 \quad (11a)$$

$$(x - x_2)^2 + (y - y_2)^2 + (z - z_2)^2 = r_2^2 \quad (11b)$$

$$(x - x_3)^2 + (y - y_3)^2 + (z - z_3)^2 = r_3^2 \quad (11c)$$

$$(x - x_4)^2 + (y - y_4)^2 + (z - z_4)^2 = r_4^2 \quad (11d)$$

where:

- the microphone (target) in the unknown position is at the coordinates  $(x, y, z)$ ;
- the centers of the four spheres (i.e. the positions of the four loudspeakers) are in the known positions with coordinates  $(x_1, y_1, z_1)$ ,  $(x_2, y_2, z_2)$ ,  $(x_3, y_3, z_3)$  and  $(x_4, y_4, z_4)$ ;
- the distances between the four loudspeakers and the target, i.e. the rays of the four spheres, are respectively  $r_1$ ,  $r_2$ ,  $r_3$  and  $r_4$ .

The solution of the system of eq.11a, 11b, 11c and 11d) is explained in detail in the Appendix.

The measurement of the four distances between the grid and the microphone is carried out by simultaneously emitting from the four loudspeakers, four MLS (Maximum Length Sequence) pseudo-random audio signals. MLS signals have an audio spectrum similar to the white noise and are commonly used in the field of the acoustic such as the test of noise barriers (Garai et al., 2014; Garai and Guidorzi, 2015). The loudspeakers emit different MLS signals, with the same time length and orthogonal to each other. Thanks to the properties of the MLS sequences (Borish and Angell, 1983; Rife and Vanderkooy, 1989; Vanderkooy, 1994), it is possible to distinguish the four different signals at the microphone even if they are emitted simultaneously. Using the Fast Hadamard Transform (FHT) algorithm, four different impulse responses are obtained from the audio signals sampled by the microphone, as shown in Fig.3 (c). From the timing of the first peak on the responses, it is possible to measure the arrival time of the sound from the four loudspeakers to the microphone. The generic distance,  $s$ , traveled by a sound wave in air between a loudspeaker and the microphone is calculated with the formula:

$$s = t \cdot c \text{ (m)} \quad (12)$$

where  $t$  is the flight time (in seconds) determined by the first peak of the impulse response, as described above, and  $c$  is the speed of sound in air depending on the temperature according to the formula:

$$c = 331.6 + 0.6 \cdot T \text{ (m/s)} \quad (13)$$

where  $T$  is the air temperature ( $^{\circ}\text{C}$ ).

MLS signals are immune to background noise, and then measurements can be made in noisy environments also. A necessary condition for the application of the methodology is that the loudspeakers must be in sight of the microphone, in order to avoid the 4 loudspeakers must be properly placed so do not have inter-visibility problem. Small obstacles, (e.g. thin branches and leaves) are not a problem and have not created issues during the tests in the greenhouse.

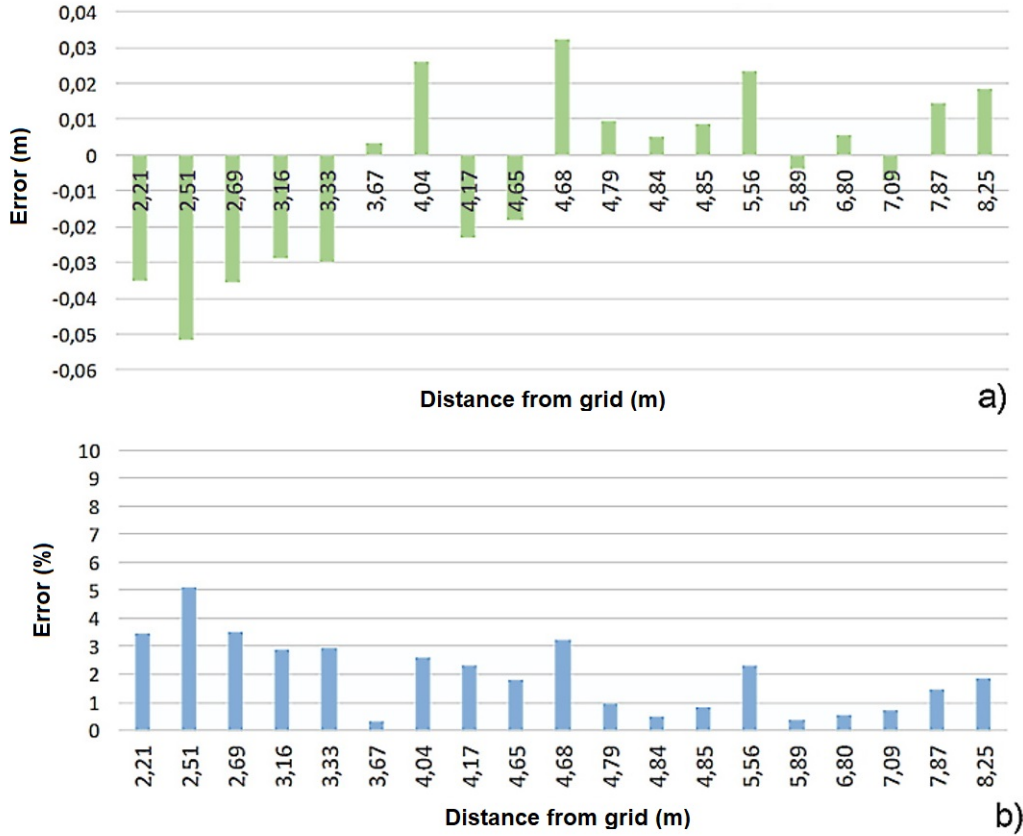


Figure 4: **a)** Measurement error on 1 m distance (sample rate 96 kHz); **b)** Percentage of error on distance measurements in a).

The accuracy of the measurement system depends on many factors, including the geometry of the measurement grid, the sampling rate of the sound card and the distance of the microphone from the grid. In particular, the sampling

299 rate determines the time step of the measured data and therefore the mini-  
 300 mum distance distinguishable from the peaks of the impulse responses: with  
 301 a 44.1 kHz sampling rate, the time step is 0.0104161667 ms, corresponding to  
 302 a distance of about 7.8 mm, at a sound speed of 343 m/s; at 96 kHz sampling  
 303 rate, the resolution on the distance is about 3.6 mm. However, an evaluation  
 304 of the real accuracy of the system is not simple because the data of the indi-  
 305 vidual distances are processed by the trilateration algorithm (searching for the  
 306 solution of the system of Equations 11a, 11b, 11c and 11d). In order to have  
 307 an assessment of the percentage error on the 3D position detected, a series of  
 308 measurements, allowing a statistical analysis, were carried out, measuring the  
 309 exact length of 1 meter at different distances from the loudspeaker grid, with  
 310 various combinations of sampling rates. It has been found that, employing a  
 311 1 m x 1 m grid, the detection system works correctly inside an area of about  
 312 10 m in each spatial direction, starting from the grid. Probably, by increasing  
 313 the size of the grid, it should be possible to extend this range. At a sample  
 314 rate of 96 kHz, as can be seen in Figure 4 a), for the positions at least 3 meters  
 315 away from the grid, the absolute error is generally less than 3 cm. The average  
 316 error, over all distances, is less than 2%, with a standard deviation of 2.34 cm.  
 317 The accuracy of the positioning system therefore can be considered suitable  
 318 for the type of measurements, realized in the present work.

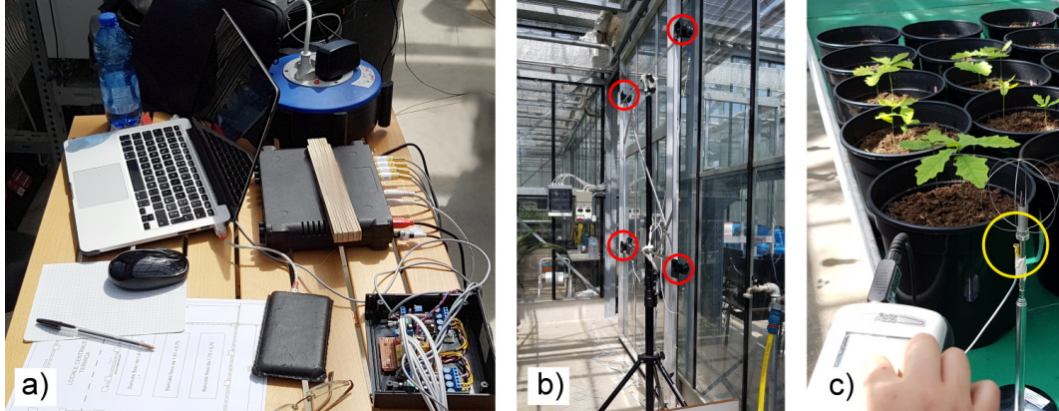


Figure 5: (a) Measurement system (computer, soundcard, amplifiers); (b) grid with loudspeakers; (c) particular of the microphone attached to the thermal probe.

319 Figure 5 shows the components of the positioning system: Fig 5 a) depicts  
 320 the computer with the software that generates the MLS signals, samples the  
 321 signal from the microphone, performs the trilateration calculations and saves  
 322 the data. In Fig.5 a) the sound card and the electronic cards with the amplifiers  
 323 for the loudspeakers are also visible. In Fig.5 b), the grid with the loudspeakers  
 324 is shown. In Fig.5 c) the microphone attached to the anemometer is shown.  
 325 The fixed distance between the microphone and the thermal sensor has been  
 326 taken into account in the assessment of the positions.



### 2.3. Numerical model validation

Twenty four locations have been defined in the cultivation area, at three different levels, e.g. 1.0 m , 1.7 m and 3.0 m.

The numerical model of the case study has been validated against the collected experimental data. In the first simulation, the average of the solar radiation and wind velocity values collected during the whole experimental campaign, have been set as boundary conditions. The diffuse solar radiation value has been estimated by the solar calculator included in Ansys Fluent, on the basis of the geographical coordinates of the site, day and hour of the beginning of the measurements (23/04/2018, 11:30 am, local time). The direct solar radiation data shows a significant variation during the period of the experimental campaign, as showed in Figure 6. In fact, Figure 6 shows variation values, even higher than  $300 \text{ W/m}^2$  in one hour. The solar radiation can significantly affect the indoor airflow distribution in a naturally ventilated greenhouse and then an approach adopting the average value could be too simplified.

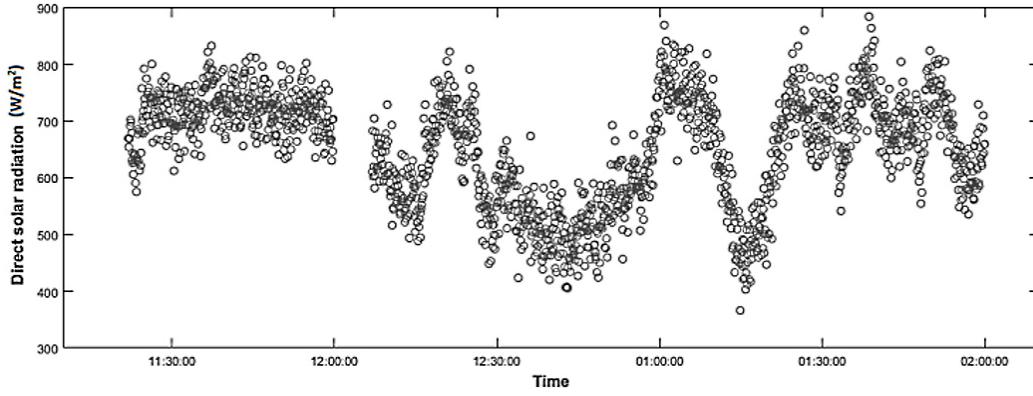


Figure 6: Direct solar radiation recorded by the pyranometer located in the proximity of the greenhouse.

Then, the direct solar radiation, averaged in a period of 15 minutes, has been used in the simulations. Figure 7 shows the comparison between the velocity values measured in the greenhouse and those obtained by the CFD simulation for the twenty four different positions.

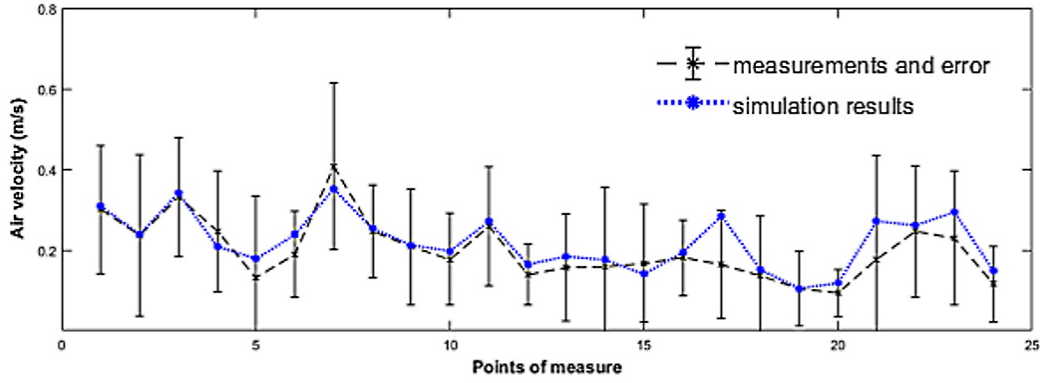


Figure 7: Comparison between measured air velocities and CFD simulation results.

The Figure 7 shows a very good agreement between the numerical results and the experimental measurements, with very low value of root mean square error (RMSE) that, calculated on the total set of measurements, results equal to 0.14 m/s.

#### 2.4. Scenarios and combinations investigated

The solar radiation could significantly affect the indoor microclimate conditions of a greenhouse during the sunny days, especially in Mediterranean climate. Moreover, as showed before, the solar radiation can vary considerably from hour to hour, the radiation value assumed in the simulation can strongly influence the numerical results. Then, in order to have results representative of the typical conditions of the site during the hot season, the weather data collected during the whole summer season 2017 have been considered. Two representative conditions have been chosen. The first condition considers a strong direct solar radiation with low wind velocity. The second assumes a moderate direct solar radiation with high wind velocity. The first condition corresponds to peaks of solar radiation intensity, while the second intends to evaluate the typical trend of the indoor parameters during the summer season. Each condition has been analyzed by assuming two different representative wind directions, i.e. North-West and South-East, providing four representative ventilation scenarios for the structure at hand.

The cases have been performed considering the implementation of three different shading screens with different geometrical and radiation characteristics, (see Santolini et al. (2019)). The shading screens are placed inside the cultivation area in three different positions: one is horizontally located at about 4.0 m height; one is laterally placed close to the lateral vent and one is located in the back of the room, close to the back wall (see Fig. 8). The three different screens are characterized by different texture (variations of porosity and inertial coefficient) but they have similar radiative properties.

The effects of the presence of the screens have been investigated in terms of both entering solar radiation and ventilation efficiency. The sixteen combinations of inlet velocity and solar radiation, summarized in Table 4, have been



Table 4: Summary of the 16 combinations investigated in this work:  $T_{initial}$  is the defined initial temperature, IR is the initial direct solar radiation value and  $v_{friction}$  is the friction velocity considered for the wind profile definition.

Scenario	$T_{initial}$ ( $^{\circ}\text{C}$ )	IR ( $\text{W}/\text{m}^2$ )	$v_{friction}$ (m/s)	Wind direction	Screen	Combinations
1	22.8	794.5	6.3	NW	No screen	1
					H3467	2
					H4215	3
					H5220	4
2	22.8	794.5	6.3	SE	No screen	5
					H3467	6
					H4215	7
					H5220	8
3	30.8	1030	2	NW	No screen	9
					H3467	10
					H4215	11
					H5220	12
4	30.8	1030	2	SE	No screen	13
					H3467	14
					H4215	15
					H5220	16

obtained by crossing four scenarios and four shading assumptions (i.e. the no screens condition and three different screens). The wind directions North-West (NW) and South-East (SE) in Table 4 has been obtained from the statistical analysis of the wind data available for 2017. They represent the direction more representative for the summer season.

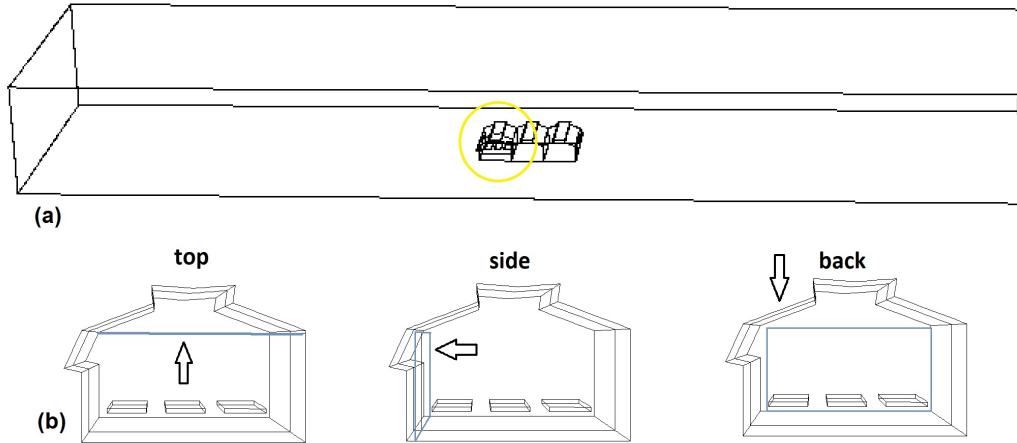


Figure 8: Image of the simulation domain and the screens positions: (a) is the simulation domain with the SE span of the greenhouse highlighted in yellow; (b) are the three positions of the screens inside the cultivation area of the SE span, highlighted in grey.

For all the sixteen combinations analyzed, the indoor environmental conditions in the productive area of the span highlighted in Figure 8, have been evaluated and reported in the following section.

### 3. Results and Discussion

The indoor velocity distribution obtained within the greenhouse, for the Scenario 1 (i.e. combinations from 1 to 4) are shown in Figure 9, by means of a vertical section based in the middle of greenhouse.

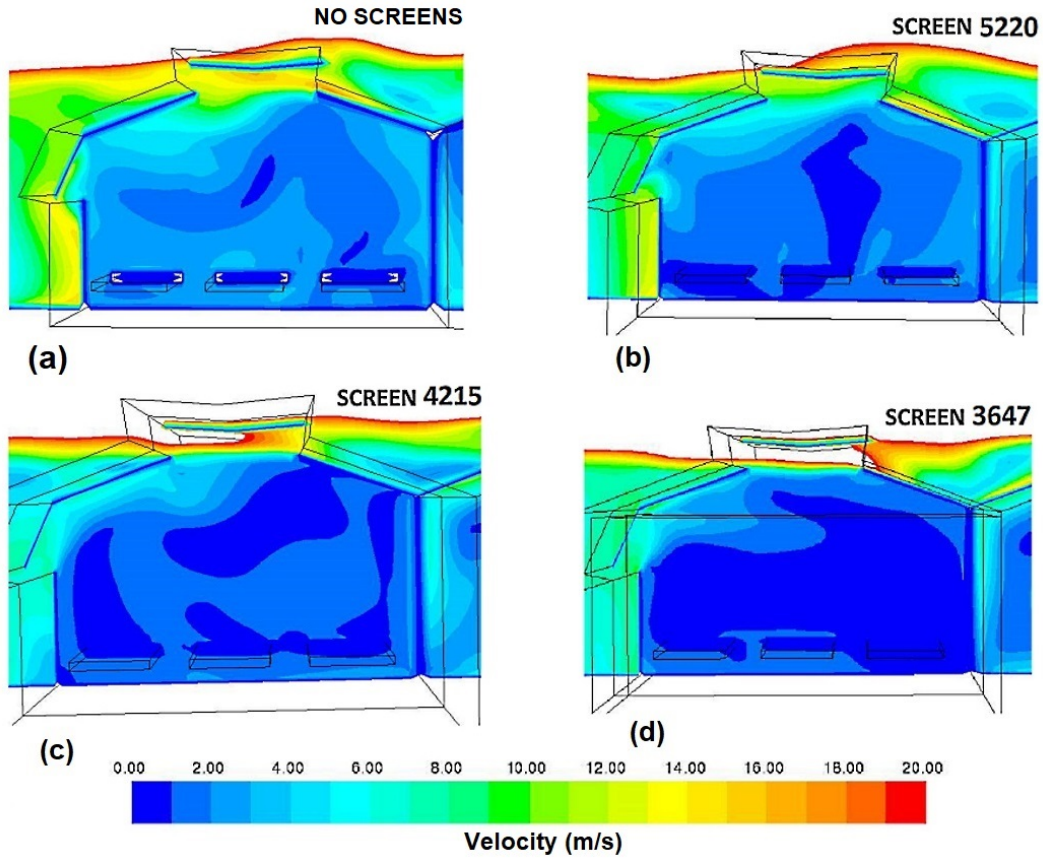


Figure 9: Contour of the air velocity magnitude distribution, on the middle vertical section of the cultivation area for the Scenario 1: (a) Combination 1; (b) Combination 2; (c) Combination 3; (d) Combination 4.

Figure 10 presents analogous results but for the Scenario 2. These scenarios are characterized by similar outdoor conditions but differ in the wind direction. The contour maps in Fig. 9 and 10 show the strong dependence of the velocity distribution from the presence and, then from the type of screen. As also obtained in other works, e.g. (Santolini et al., 2018), the presence of the shading devices strongly affects the airflow distribution inside the structure. The main effect of the screens, on the ventilation, is to reduce the mixing and the velocity magnitude, also in case of strong solar radiation. Smaller is the grid dimension of the screen and higher is the number of the impermeable strips respect to the number of the porous one in the texture, generally lower is the indoor magnitude velocity and enlarged are the areas of the section with velocity almost zero, as clearly visible in Figure 9.

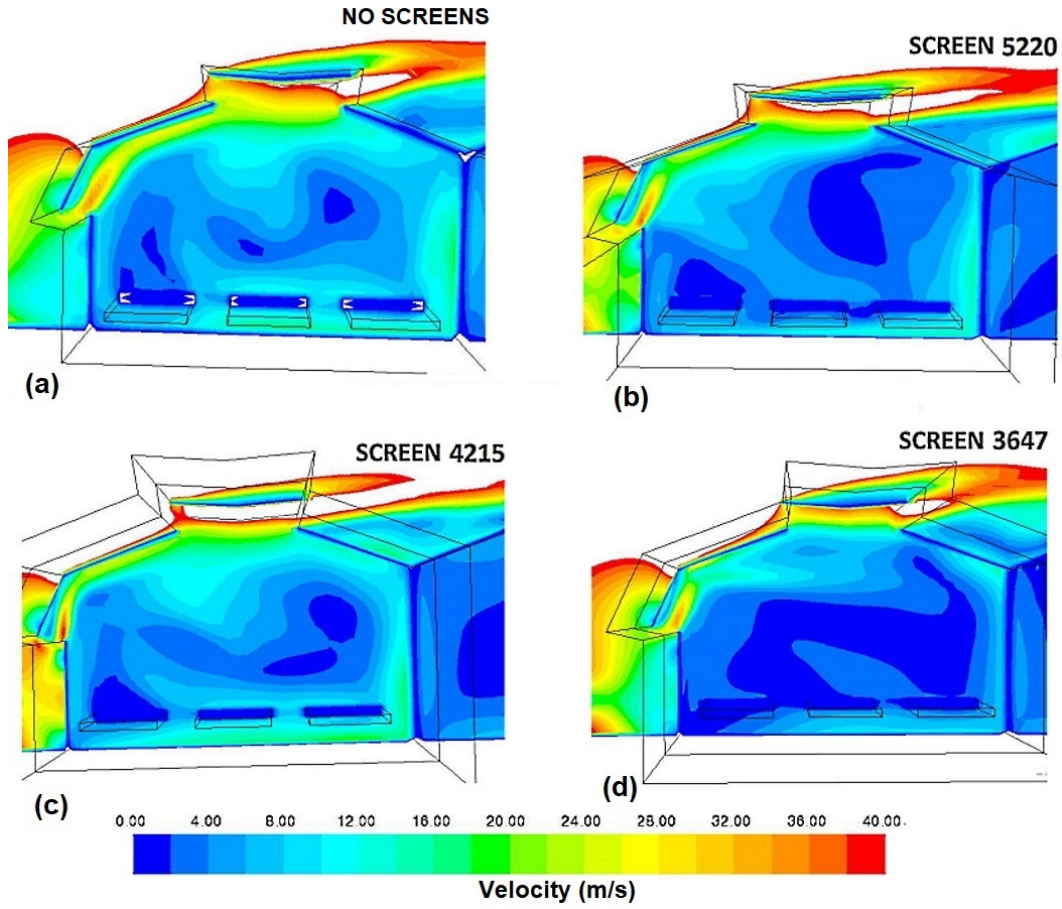


Figure 10: Contour of the air velocity magnitude distribution, on the middle vertical section of the cultivation area for the Scenario 2: (a) Combination 5; (b) Combination 6; (c) Combination 7; (d) Combination 8.

However, the negative action of screens, reducing the air velocity magnitude, doesn't raise if the incoming air velocity increases, as visible from the comparison of the Scenario 1 and Scenario 2. This aspect highlights and confirms that inertial coefficient has a reduced impact on the airflow through the porous surface when the air velocity in inlet is increasing, as supposed in Santolini et al. (2019). The results obtained for the case with wind blowing from South-East (Scenario 2), where the wind has strong magnitude and it is perpendicular to lateral and roof vents. In this case, the effect of the screens, on the velocity field, are considerably less relevant than in Scenario 1. In Figure 10, the variation of the air velocity magnitude and distribution due to the presence of the screens is limited in all cases, particularly in presence of H4215. Analogous air velocity contours have been obtained, obviously with different magnitude order, for the Scenarios 3 and 4, and are not reported here for the sake of paper brevity.

On the contrary, the temperature distributions inside the cultivation area, obtained for the two Scenarios 1 and 2, are very different. Figures 11 and 12 show the temperature distribution obtained on a vertical section, for Scenario

1 and 2, respectively. Both scenarios show a rather homogeneous temperature in the cultivation area, thanks to the presence of the screens.

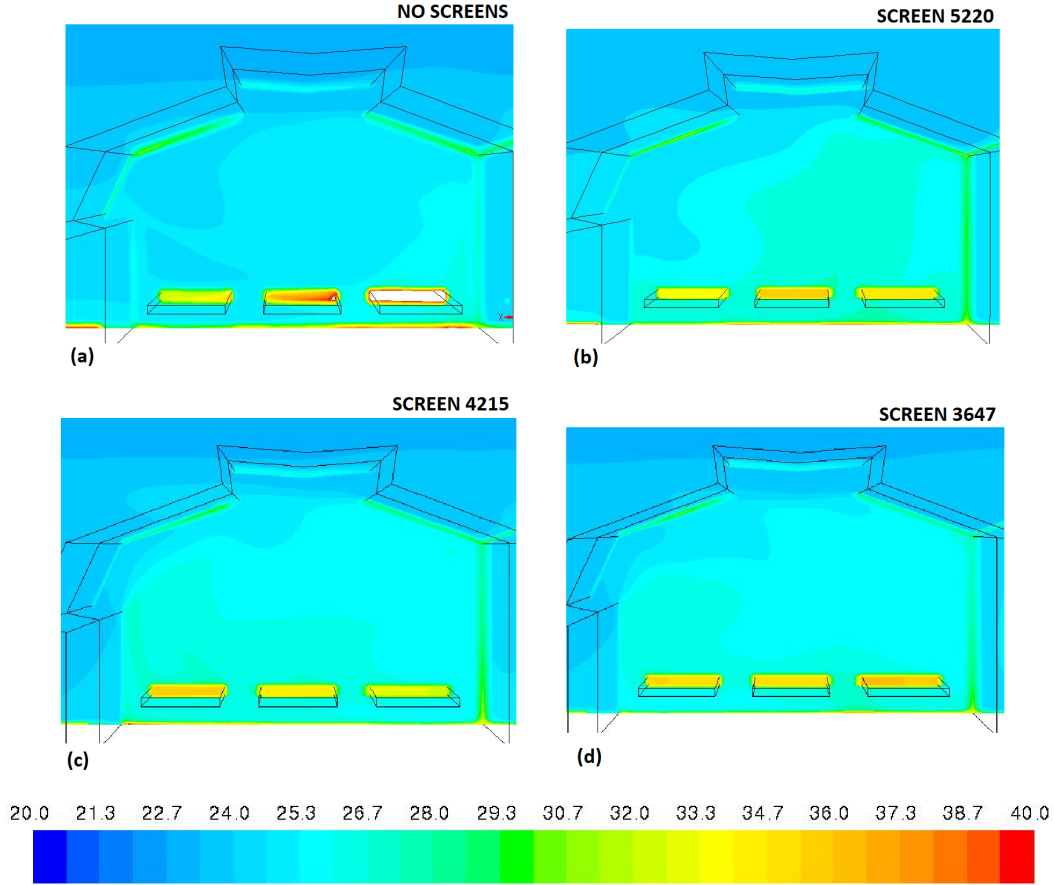


Figure 11: Contour of the temperature distribution, on the middle section of the cultivation area, of Scenario 1: (a) Combination 1; (b) Combination 2; (c) Combination 3; (d) Combination 4.

However, the two Scenarios show very different temperature reduction ranges, within the cultivation area. The average temperature in Scenario 1, in the cultivation area, is about 26.5 °C and is 23.5 °C in Scenario 2. Then, the difference in terms of temperature reduction, between the two Scenarios, is about 3 °C. In fact, in the Scenario 2 the wind velocity contribution in the cultivation area is more consistent. Another interesting aspect, emerging in the Scenario 2, is the effective mitigation of the temperature value of the first bench on the left, close to the lateral window, provided by the shading devices. A similar situation is visible also in the Scenario 1, where the worst condition in terms of high temperature is provided by the internal bench (right bench in the Figures 11), close to the internal wall separating two different spans, and located far from the lateral window.

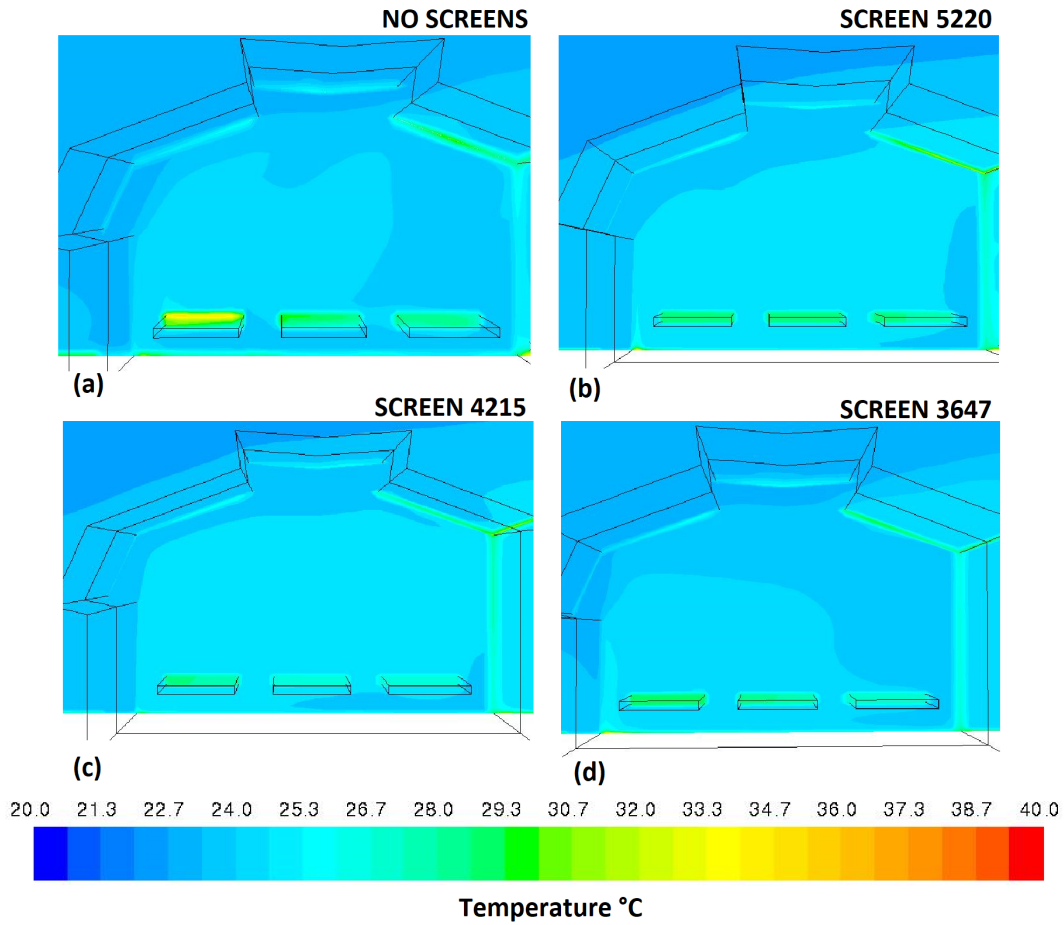


Figure 12: Contour of the temperature distribution, based on the middle section of the cultivation area, of Scenario 2: (a) Combination 5; (b) Combination 6; (c) Combination 7; (d) Combination 8.

Figure 11 and 12 show that shading devices will provide potential better conditions for the crop growth because the temperature distribution is more homogeneous in presence of the screens. The shading devices have a positive effect not only in the cases of strong wind and limited solar radiation but also in those cases with high solar radiation. Indeed, Figures 13 and 14 show the temperature distribution on the middle vertical section, for Scenario 3 and 4, respectively. The temperature distribution obtained for Scenario 3 shows homogeneous distribution together with average temperature values, higher than temperature in Scenario 4. This outcome can be attributable to the reduced action of the natural ventilation in the heat removal, due to both, the unfavourable wind direction and reduced wind magnitude, in synergy with the negative consequences of the screens presence.



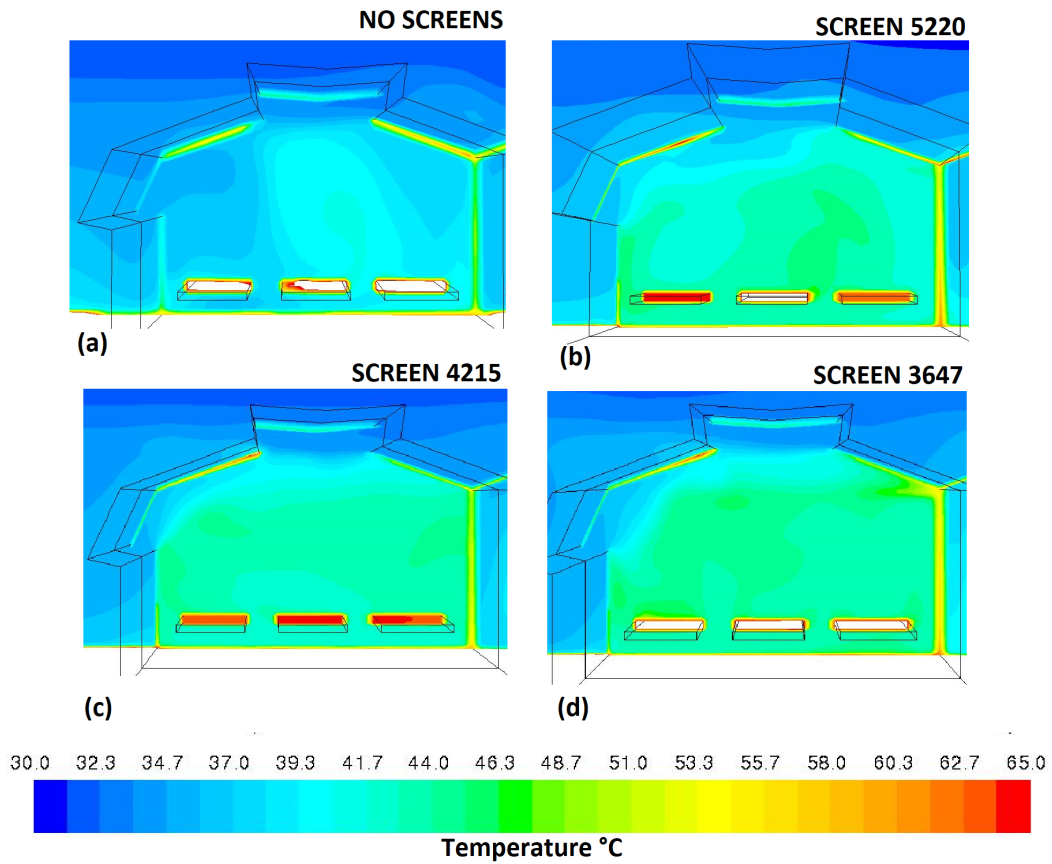


Figure 13: Contour of the temperature distribution, based on the middle section of the cultivation area of Scenario 3: (a) Combination 9; (b) Combination 10; (c) Combination 11; (d) Combination 12.

On the other side, in the Scenario 4, with the wind blowing from South-East direction, the shading devices allow to create a rather homogeneous temperature distribution, around 35-37 °C, inside the structure, without the consistent temperature increase showed in Figure 13 for the Scenario 3.

Focusing on the main aim of the use of the shading devices that is to maximize the plant growth, two different conditions are important: the temperature over the benches and the velocity value and distribution around the crops.

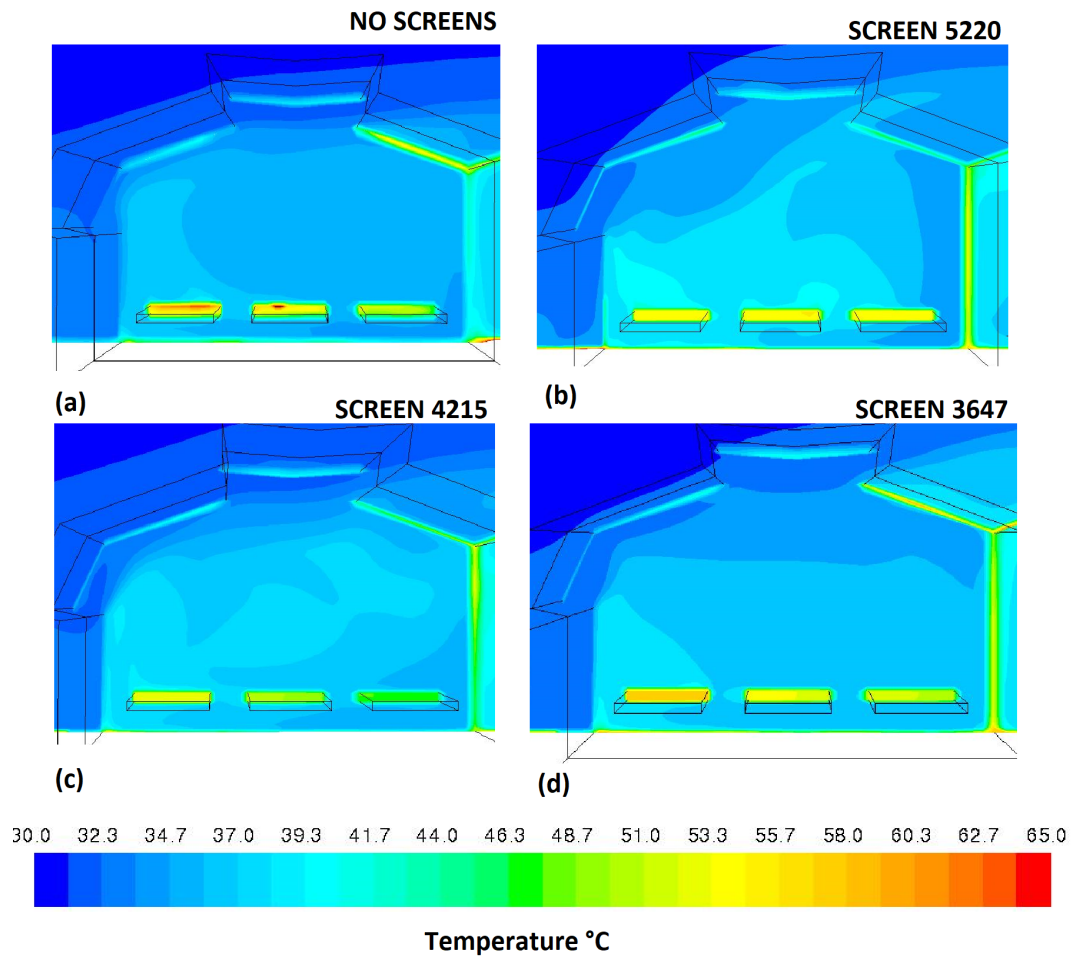


Figure 14: Contour of the temperature distribution, on the middle section of the cultivation area, of Scenario 4: (a) Combination 13; (b) Combination 14; (c) Combination 15; (d) Combination 16.

452 To this regard, firstly, the Scenarios 3 and 4 have been analysed. In Figure  
 453 15, the temperature distribution, at a distance of 10 cm from the benches, is  
 454 presented for Scenarios 3 and 4. The Figure 15 shows the remarkable benefits  
 455 of the introduction of the shading devices, in terms of both temperature level  
 456 and distribution, close to the crops.

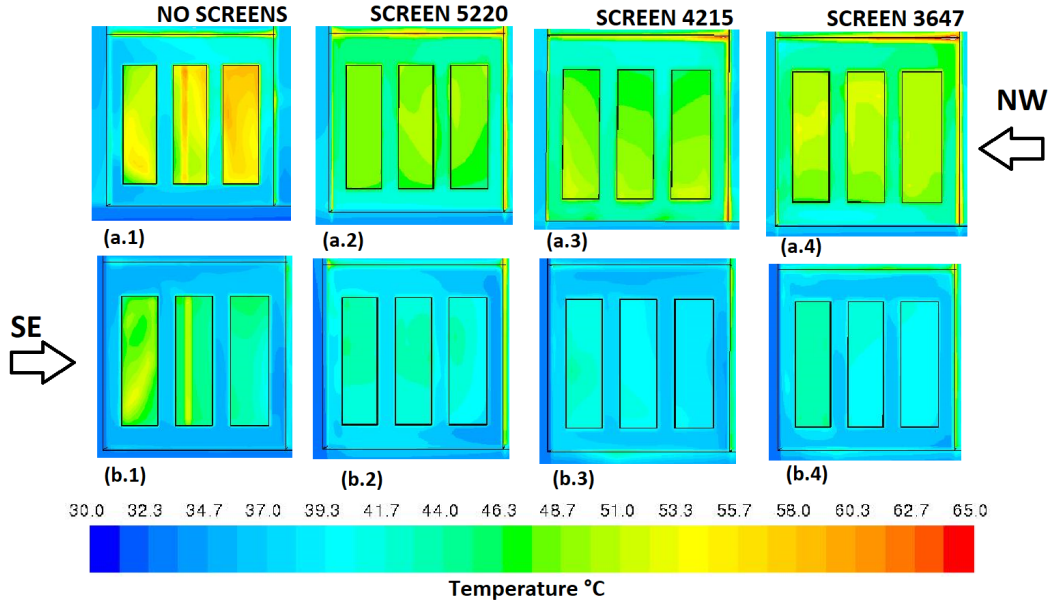


Figure 15: Contour of the temperature at the crop level: (a) Scenario 3; (b) Scenario (4).

In the case without screens (see No screens case), the first left bench, on Scenario 3, and the third left bench, on Scenario 4, show the highest temperature at the crop level together with a poorly homogeneous distribution. The temperature distribution becomes homogeneous only in the sub cases with screens. Obviously, the positive impact of the screens depends on type of screen and on wind direction. The influence of every type of screen, with wind blowing from NW, can be considered similar in terms of temperature magnitude, but has slightly different temperature distributions. In presence of the screens H5220 and H3647, the temperature distribution is rather homogeneous over all the cultivation benches. On the contrary, the screen H4215 creates an area, closer to the back wall of the greenhouse, with a slightly greater temperature. Different conditions can be noticed in case of wind blowing from SE, because the screens H4215 and H3647 have a stronger influence in reducing the temperature values, if compared to H5220 screen.

When the wind magnitude is higher and the solar radiation effects is limited, the temperature distributions over the benches are similar if screens are introduced in the building, as showed in Figure 16. For these cases, the different screens have similar influence on temperature magnitude and distribution.



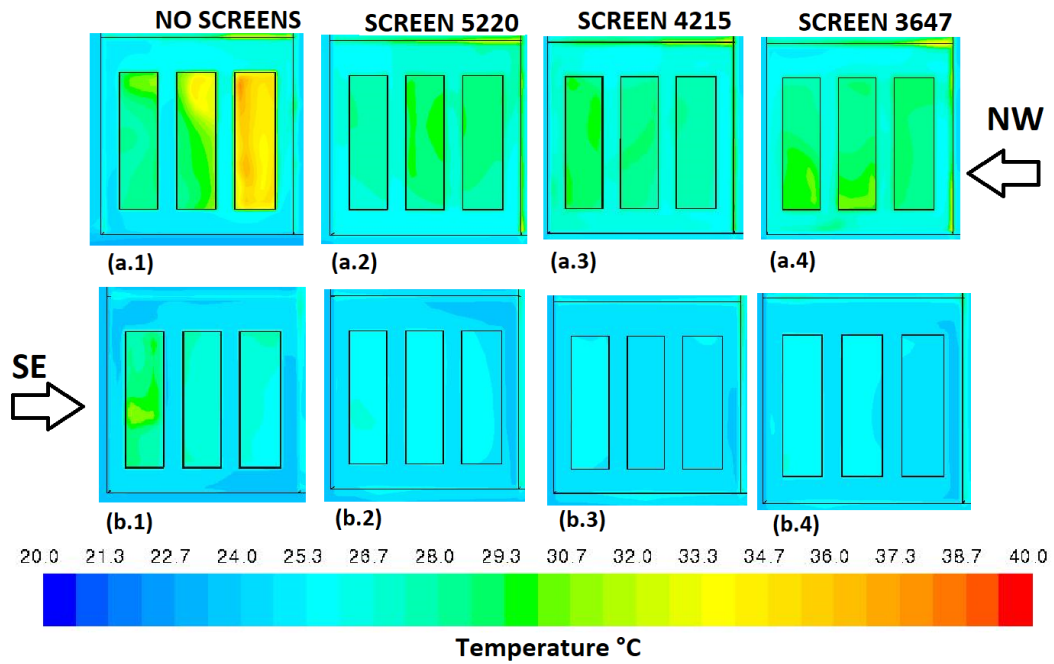


Figure 16: Contour of the temperature at the representative level: (a) Scenario 1; (b) Scenario 2.

Moreover, the temperature mitigation is less dependent on wind direction. These results are analysed in detail in Figure 17. The values reported in Figure 17 are the peak values obtained for each one of the 16 combinations at the level of 10 cm over the benches. The temperature reductions reported, instead, are obtained from the values in Figure 16 as difference between the value of the case considering a particular screen and the "no screens" case.

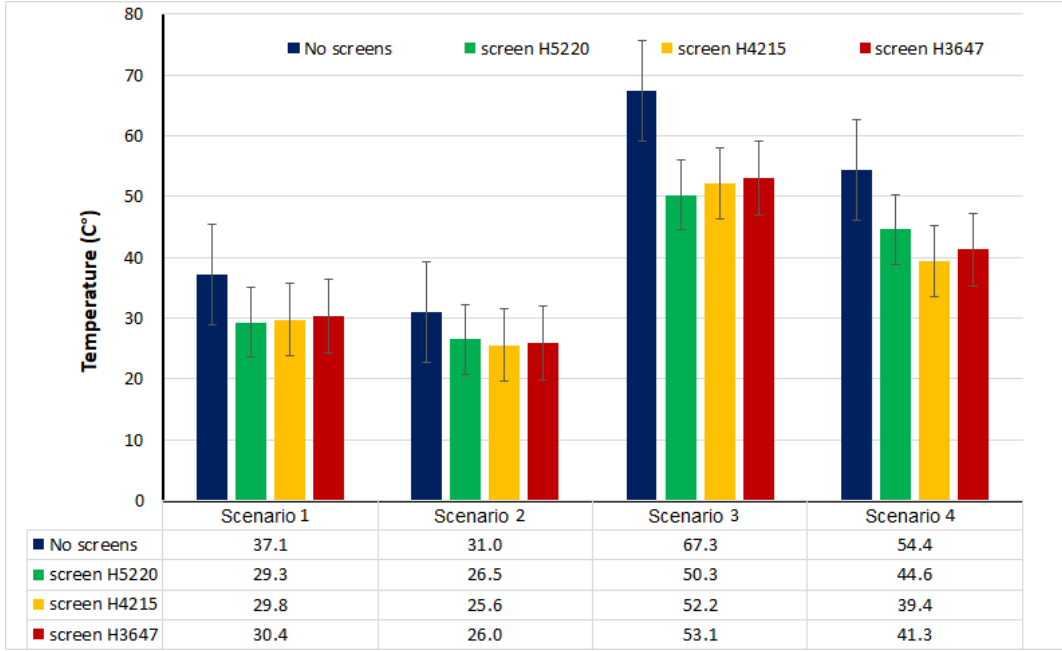


Figure 17: Peak temperature obtained for the various scenarios 10 cm over the bench level.

The H5220 screen allows to obtain a temperature reduction value ranging from 4.5 °C and 17 °C, with an average value around 9.8 °C. The temperature reduction achievable with the H4215 and H3647 are similar: it ranges from 4.5 °C to about 15 °C with average value about 5 °C. The temperature mitigation index,  $\delta_T$ , have been calculated by Eq. 14 for the three screens in the four scenarios, as reported in Table 5. The mean value for each screen has been estimated in order to identify a single index representative of the mitigation effect of each screen.

$$\delta_T = \frac{T_{max,noscreen} - T_{max,screen}}{T_{max,noscreen}} \quad (14)$$

where  $T_{max,noscreen}$  is the peak of temperature in a specific scenario without screen and  $T_{max,screen}$  is the peak of temperature in a specific scenario with a specific screen.

Table 5: Quantified temperature mitigation operated by each screen in a specific scenario by means of the  $\delta_T$  index.

	H5220	H4215	H3647
Scenario	$\delta_T$	$\delta_T$	$\delta_T$
1	0.21	0.197	0.18
2	0.16	0.174	0.16
3	0.253	0.224	0.211
4	0.18	0.276	0.241
mean	0.2	0.22	0.2

The screens show similar mitigation effects in three of the four scenarios. However, in the scenario 4 (high solar radiation and moderate wind velocity) the H5220 screen is characterized by a significantly important effect which is 1.5 and 1.3 times higher than the case with H4215 and H3647 respectively. The temperature reduction obtainable from each screen strongly depends on the external climate conditions. In fact, the final mitigation index shows marginal differences between the three devices, confirming anyway that H5220 and H3647 are slightly more efficient.

Finally, the analysis of the temperature trends for the various combinations along the vertical axis, can be useful to evaluate the effects of the screen presence and to assess the temperature homogeneity for increasing level in order to estimate the possible effects on crops with different height. The peak temperatures detected for different levels from 10 to 30 cm over the benches are depicted in Figure 18 for Scenarios 3 and 4.

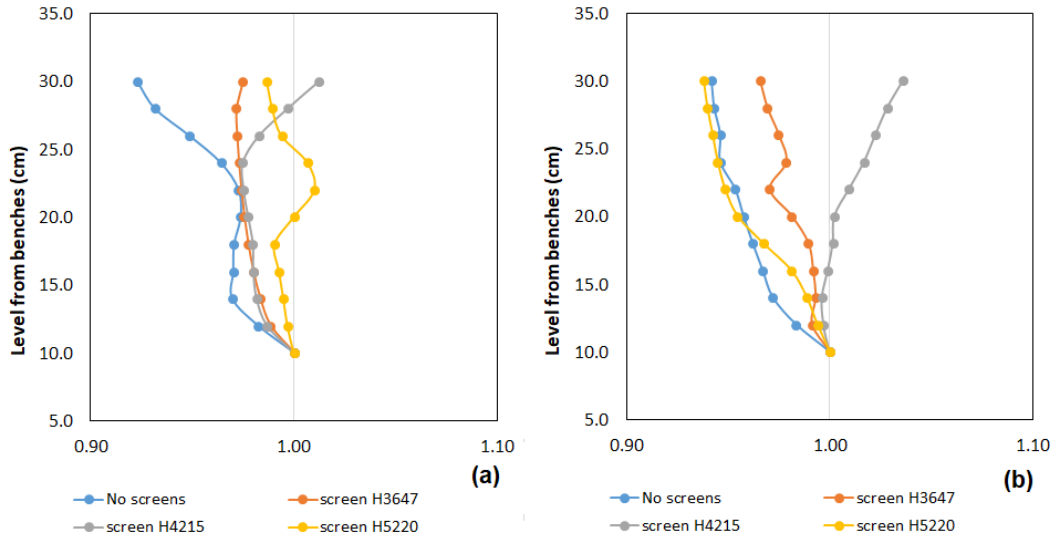


Figure 18: Comparison of the peak temperature trends for different combinations at different heights over the benches: (a) Scenario 3 and (b) Scenario 4.

In the figure, the values are normalized by the value observed at the reference level explained before and equal to 10 cm over the benches. The first graph shows the peak temperatures trends of the Scenario 3. The temperatures of the combinations with shading devices have, in general, a more homogeneous trends if compared with the case without screens ("No screens" case) since the values are usually closer to the unitary value.

Analogously, in Figure 18(b) are showed the trends for the Scenario 4. Also in this case, the adoption of the screens, improves the air temperature homogeneity at all the levels investigated, confirming the effectiveness of the shading devices in the mitigation of this type of problem in the greenhouse cultivation. Similar consideration could be found for the Scenario 1 and 2. They are not reported here for brevity reasons.

Since the considerations for the optimal conditions for plant growth usually must take into account temperature and air velocity distributions, the temperature and the air velocity magnitudes have been compared based on their average values, obtained for seven levels in the cultivation area. Then, seven sections from 10 to 30 cm over from the cultivation benches have been considered for the analysis. In Figure 19, blue bars are referring to the temperature values while red bars refer to the air velocity magnitudes.

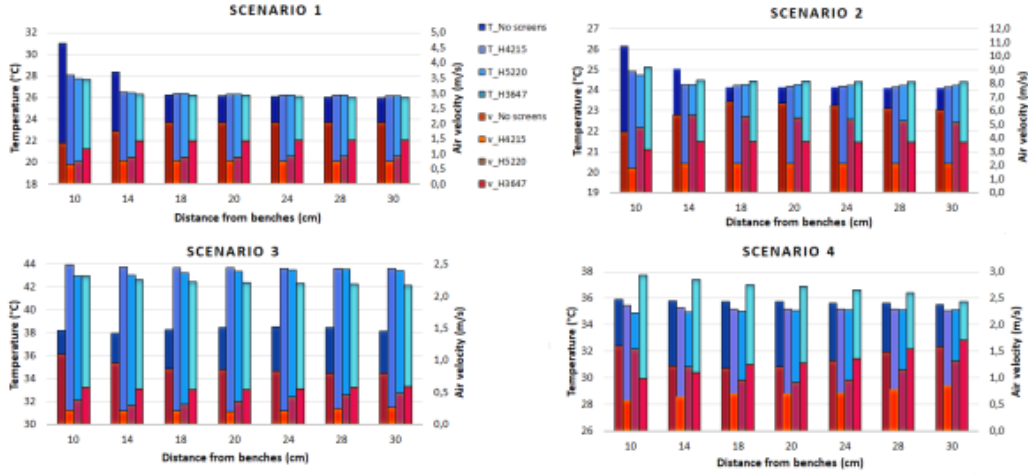


Figure 19: Comparison between the results of averaged temperature and air velocity, at several levels, for all scenarios and combinations.

In the Scenario 1, a considerable temperature reduction is provided by the three screens in the first and in the second section. On the other hand, the air velocity is considerably affected by the screens presence. In this scenario, the H3647 screen demonstrates the best mitigation effects on the temperature, maintaining a good ventilation, i.e. a good air velocity, in the cultivation area. Similar results can be noticed for the Scenario 2, where the H3647 screen shows good performances. However, in this scenario, the best temperature reduction with highest level of ventilation is usually provided by the H5220 screen. On the contrary, in case of strong incident solar radiation and wind blowing with low velocity from a critical direction, i.e NW, (scenario 3), all the screens demonstrates to be ineffective on the temperature while worsening the air flow distribution. Finally, in Scenario 4, the H4215 and H5220 are able to provide a good improvement of the temperature values. On the contrary, in this scenario, the H3647 screen has globally a negative performance. In this last case, the best performance is to attribute to the H4215 screen. Considering the results as a whole, the screen H4215 and H5220 demonstrated similar effects on the indoor environment for three cases out of four, despite their significant differences in texture and physical properties. Concluding, the shading devices with a with visible porosity in the texture and characterized by good radiative performances represent the best shading solution for the analysed case study. A screen with low permeability like the H5220 gives better performances if

used in situations where the wind does not hit the wall directly. On the other hand, in situations where the wind hits the walls directly, screens with higher permeability like the H4215 give better performances.

## 4. Conclusions

The shading devices are one of the most used solution, in protected crop structures, to mitigate the effects of solar radiation, especially in the sunny days during the hot season in Mediterranean area. They are usually placed internally, over the cultivation area, in order to positively affect the incident radiation and to create better conditions for the crop growth. In fact, the presence of shading devices can significantly modify the indoor environmental conditions. However, they affect not only the solar radiation but also the air flow distribution, because they can considerably reduce the indoor air velocity, especially if they have a low porosity texture. In this paper, the combinations of the reduction of the solar radiation with the modification of the flow velocity given by three different shading screens have been analysed. Different outdoor environmental conditions have been considered, in order to consider combinations of low solar radiation and different wind velocity and directions. The choice of a specific shading device is very important because it allows to create more suitable conditions for the crop cultivation. The same considerations can be performed on the air flow distribution. The indoor temperature distribution has been obtained for different scenarios, in term of maximum temperature achieved together with a low variability above the crops. The performances of each screen have been compared and correlated with the environmental conditions. The results show that screens with low permeability like the H5220 and the H4215 give optimal temperature mitigation together with a uniform temperature distribution above the crops. However, screens with higher permeability give better performances in situations where the wind hits the walls directly. The best choice, for the case considered in this paper, is the H4215, *i.e.* a screen with a permeability equal to  $0.58 \text{ m}^{-1}$ . This means that the choice of the best screen must be done considering also the most frequent conditions in terms of wind directions with respect to orientation and position of the windows in the greenhouse.

## Appendix

The method of solving the 3D trilateration problem used in this work, *i.e.* how to find the position in the space of a target point knowing its distance from four known points, is now enunciated. To find the intersection point of the four spheres it is necessary to solve a system of four equations with four unknowns. To simplify the computational procedure, making it usable even in poor computers or micro-controllers, it will be solved a system of three equations in three unknowns, taking into account only three of the four spheres,

587 obtaining in this way two possible solutions. Applying this procedure to the  
 588 four possible combinations of three of the four spheres, a unique solution will  
 589 be obtained.

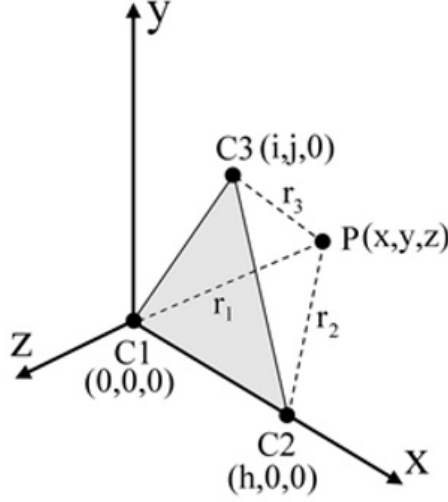


Figure 20: Three spheres centers ( $C_1$ ,  $C_2$ ,  $C_3$ ) and target point (P).

590 In the equations 11a,11b and 11c the coordinates ( $x$ ,  $y$ ,  $z$ ) describe the  
 591 unknown position of the microphone P (target); the coordinates ( $x_1$ ,  $y_1$ ,  $z_1$ ),  
 592 ( $x_2$ ,  $y_2$ ,  $z_2$ ) and ( $x_3$ ,  $y_3$ ,  $z_3$ ) describe the known positions of the centers of the  
 593 three spheres  $C_1$ ,  $C_2$  and  $C_3$  considered for the calculations; the radii  $r_1$ ,  $r_2$   
 594 and  $r_3$  are the known distances (radii of the spheres  $C_1$ ,  $C_2$  and  $C_3$ ) between  
 595 the target position P and the centers of the mentioned spheres.

596 The system is described by the equations:

$$(x - x_1)^2 + (y - y_1)^2 + (z - z_1)^2 = r_1^2 \quad (15a)$$

$$(x - x_2)^2 + (y - y_2)^2 + (z - z_2)^2 = r_2^2 \quad (15b)$$

$$(x - x_3)^2 + (y - y_3)^2 + (z - z_3)^2 = r_3^2 \quad (15c)$$

599 A new coordinate system is now defined, as shown in Figure 20, used  
 600 temporarily to solve the system of equations in 15a15b15c. The origin of the  
 601 new system, at coordinates (0,0,0), is placed at the center of sphere  $C_1$ ; the  
 602 center of sphere  $C_2$  is placed at ( $h$ ,0,0); the center of sphere  $C_3$  is placed at  
 603 ( $i$ , $j$ ,0). The centers of the spheres are therefore all on the same plane xy.

604 The vectors that define the base of the new coordinate system are:

$$\hat{e}_x = \frac{\bar{p}_2 - \bar{p}_1}{\|\bar{p}_2 - \bar{p}_1\|} \quad (16a)$$

$$\hat{e}_y = \frac{(\bar{p}_3 - \bar{p}_1) - \hat{e}_x \cdot (\hat{e}_x \cdot (\bar{p}_3 - \bar{p}_1))}{\|(\bar{p}_3 - \bar{p}_1) - \hat{e}_x \cdot (\hat{e}_x \cdot (\bar{p}_3 - \bar{p}_1))\|} \quad (16b)$$

$$\hat{e}_z = \hat{e}_x \times \hat{e}_y \quad (16c)$$

The centers of the three spheres  $C_1$ ,  $C_2$  and  $C_3$  are defined, in the new coordinate system, as:

$$C_1 : \bar{p}_1 = (x_1, y_1, z_1)$$

$$C_2 : \bar{p}_2 = (x_2, y_2, z_2) = \bar{p}_1 + \hat{e}_x h$$

$$C_3 : \bar{p}_3 = (x_3, y_3, z_3) = \bar{p}_1 + \hat{e}_x i + \hat{e}_y j$$

being:  $h = \hat{e}_x \cdot (\bar{p}_2 - \bar{p}_1)$ ,  $i = \hat{e}_x \cdot (\bar{p}_3 - \bar{p}_1)$ ,  $j = \hat{e}_y \cdot (\bar{p}_3 - \bar{p}_1)$ .

The equations 16a 16b 16c in the new coordinate system are:

$$(X_n)^2 + (Y_n)^2 + (Z_n)^2 = r_1^2 \quad (17a)$$

$$(X_n - h)^2 + (Y_n)^2 + (Z_n)^2 = r_2^2 \quad (17b)$$

$$(X_n - i)^2 + (Y_n - j)^2 + (Z_n)^2 = r_3^2 \quad (17c)$$

In the equations 17a, 17b and 17c, the variables  $x$ ,  $y$  and  $z$  are renamed as  $X_n$ ,  $Y_n$  and  $Z_n$  to avoid confusion with the original coordinate system. The two solutions of Eq. 17a, 17b and 17c are therefore:

$$X_n = \frac{r_1^2 - r_2^2 + h^2}{2h} \quad (18a)$$

$$Y_n = \frac{r_1^2 - r_3^2 + i^2 + j^2 - 2iX_n}{2j} \quad (18b)$$

$$Z_n = \pm \sqrt{r_1^2 - X_n^2 - Y_n^2} \quad (18c)$$

The two solutions, rewritten in the original coordinate system, are:

$$\text{Solution1} : \bar{p}_a = \bar{p}_1 + \hat{e}_x X_n + \hat{e}_y Y_n + \hat{e}_z Z_n \quad (19)$$

$$\text{Solution2} : \bar{p}_b = \bar{p}_1 + \hat{e}_x X_n + \hat{e}_y Y_n - \hat{e}_z Z_n \quad (20)$$

The two solutions found are symmetrical to the plane on which the centers of the three spheres are located. In GitHub, a C++ public domain code for the resolution according to the described method can be found. It remains to be determined which of the two solutions found is the real one. The described procedure is repeated to cover all possible combinations of intersections of four spheres, taken three at a time. The number of required combinations is ( $n =$

630 4,  $k = 3$ ):

$$\frac{n!}{k!(n-k)!} = \frac{4!}{3!(4-3)!} = 4 \quad (21)$$

631 By renaming  $S_1, S_2, S_3$  and  $S_4$  the four spheres, the possible combinations  
632 are:  $(S_1, S_2, S_3)$ ,  $(S_1, S_2, S_4)$ ,  $(S_1, S_3, S_4)$  and  $(S_2, S_3, S_4)$ . By solving the prob-  
633 lem four times, considering the above mentioned combinations of spheres, four  
634 pairs of solutions are obtained. In each pair only one exact solution exists, so  
635 by examining all four pairs of solutions, the real solution will be the one that  
636 appears in all the four cases.

## 637 References

- 638 Baille, A.. Greenhouse structure and equipment for improving crop production  
639 in mild winter climate. *Acta Horticulturae* 1999;(491):37–48. doi:10.17660/  
640 *ActaHortic*.1999.491.4.
- 641 Barbaresi, A., Maioli, V., Bovo, M., Tinti, F., Torreggiani, D., Tassinari, P..  
642 Application of basket geothermal heat exchangers for sustainable greenhouse  
643 cultivation. *Renewable and Sustainable Energy Reviews* 2020;129:109928.  
644 doi:<https://doi.org/10.1016/j.rser.2020.109928>.
- 645 Bartzanas, T., Boulard, T., Kittas, C.. Effect of vent arrangement on  
646 windward ventilation of a tunnel greenhouse. *Biosystems Engineering* 2004;.
- 647 Baxevanou, C., Bartzanas, T., Fidaros, D., Kittas, C.. Solar radiation  
648 distribution in a tunnel greenhouse. *Acta Horticulturae* 2008;801 PART  
649 2(1989):855–862. doi:10.17660/*ActaHortic*.2008.801.100.
- 650 Baxevanou, C., Fidaros, D., Bartzanas, T., Kittas, C.. Numerical simula-  
651 tion of solar radiation, air flow and temperature distribution in a naturally  
652 ventilated tunnel greenhouse. *Agricultural Engineering International: CIGR*  
653 *Journal* 2010;12(3-4):48–67.
- 654 Borish, J., Angell, J.B.. An efficient algorithm for measuring the impulse  
655 response using pseudorandom noise. *J Audio Eng Soc* 1983;31(7/8):478–488.
- 656 Boulard, T., Kittas, C., Roy, J.C., Wang, S.. Convective and ventilation  
657 transfers in greenhouses, part 2: Determination of the distributed green-  
658 house climate. *Biosystems Engineering* 2002;83:129–147.
- 659 Fatnassi, H., Boulard, T., Poncet, C., Chave, M.. Optimisation of green-  
660 house insect screening with computational fluid dynamics. *Biosystems En-*  
661 *gineering* 2006;93:301–312.
- 662 Fluent Inc, . *FLUENT 6.3 User’s Guide*, 2006.



663 Garai, M., Guidorzi, P.. Sound reflection measurements on noise barriers in  
664 critical conditions. *Building and Environment* 2015;94:752 – 763. doi:<https://doi.org/10.1016/j.buildenv.2015.06.023>.  
665

666 Garai, M., Schoen, E., Behler, G., Bragado, B., Chudalla, M., Conter, M.,  
667 Defrance, J., Demizieux, P., Glorieux, C., Guidorzi, P.. Repeatability  
668 and reproducibility of in situ measurements of sound reflection and airborne  
669 sound insulation index of noise barriers. *Acta Acustica united with Acustica*  
670 2014;100(6):1186–1201. doi:doi:10.3813/AAA.918797.

671 GitHub, . Repository page about trilateration. [https://github.com/cnm/](https://github.com/cnm/MITSensorReading/blob/master/lib/vec3d.c)  
672 [MITSensorReading/blob/master/lib/vec3d.c](https://github.com/cnm/MITSensorReading/blob/master/lib/vec3d.c). Accessed: 2019-07-14.

673 Guidorzi, P.. Three-dimensional acoustic positioning system. Jun 14, 2017.

674 He, K., Chen, D., Sun, L., Huang, Z., Liu, Z.. Analysis of the cli-  
675 mate inside multi-span plastic greenhouses under different shade strategies  
676 and wind regimes. *Korean Journal of Horticultural Science and Technology*  
677 2014;32(4):473–483. doi:10.7235/hort.2014.13156.

678 Katsoulas, N., Baille, A., Kittas, C.. Effect of misting on transpiration  
679 and conductances of a greenhouse rose canopy. *Agricultural and Forest*  
680 *Meteorology* 2001;106(3):233–247. doi:10.1016/S0168-1923(00)00211-2.

681 Kitta, E., Katsoulas, N., Savvas, D.. Shading Effects on Greenhouse Micro-  
682 climate and Crop Transpiration in a Cucumber Crop Grown Under Mediter-  
683 ranean Conditions. *Applied Engineering in Agriculture* 2012;28(1):129–140.  
684 doi:10.13031/2013.41281.

685 Kittas, C., Baille, A., Giaglaras, P.. Influence of Covering Material and  
686 Shading on the Spectral Distribution of Light in Greenhouses. *Journal of*  
687 *Agricultural Engineering Research* 1999;73(4):341–351. doi:10.1006/jaer.  
688 1999.0420.

689 Kittas, C., Bartzanas, T., Jaffrin, A.. Temperature Gradients in a Partially  
690 Shaded Large Greenhouse equipped with Evaporative Cooling Pads. *Biosys-*  
691 *tems Engineering* 2003;85(1):87–94. doi:10.1016/S1537-5110(03)00018-7.

692 Lien, F.S., Leschziner, M.A.. Assessment of turbulence-transport mod-  
693 els including non-linear rng eddy-viscosity formulation and second-moment  
694 closure for flow over a backward-facing step. *Computers and Fluids*  
695 1994;23(8):983–1004. doi:10.1016/0045-7930(94)90001-9.

696 Miguel, A.F.. Airflow through porous screens: From theory to practical  
697 considerations. *Energy and Buildings* 1998;28:63–69.

698 Miguel, A.F., Silva, A.M.. Porous materials to control climate behaviour of  
699 enclosures: An application to the study of screened greenhouses. *Energy*  
700 *and Buildings* 2000;31:195–209.

701 Miguel, A.F., Van De Braak, N.J., Bot, G.P.. Analysis of the airflow  
702 characteristics of greenhouse screening materials. *Journal of Agricultural*  
703 *and Engineering Research* 1997;67:105–112.

704 Montero, J.I., Muñoz, P., Sánchez-Guerrero, M.C., Medrano, E., Piscia,  
705 D., Lorenzo, P.. Shading screens for the improvement of the night time  
706 climate of unheated greenhouses. *Spanish Journal of Agricultural Research*  
707 2013;11(1):32. doi:10.5424/sjar/2013111-411-11.

708 Murthy, J.Y., Mathur, S.R.. Finite Volume Method for Radiative Heat  
709 Transfer Using Unstructured Meshes. *Journal of Thermophysics and Heat*  
710 *Transfer* 2008;12(3):313–321. doi:10.2514/2.6363.

711 Piscia, D., Montero, J.I., Melé, M., Flores, J., Perez-Parra, J., Baeza, E.J..  
712 A CFD model to study above roof shade and on roof shade of greenhouses.  
713 *Acta Horticulturae* 2012;952:133–140.

714 Raithby, G.D.. Discussion of the finite-volume method for radiation, and its  
715 application using 3d unstructured meshes. *Numerical Heat Transfer, Part*  
716 *B: Fundamentals* 1999;35(4):389–405. doi:10.1080/104077999275802.

717 Rife, D.D., Vanderkooy, J.. Transfer-function measurement with maximum-  
718 length sequences. *J Audio Eng Soc* 1989;37:419–444.

719 Roy, J.C., Boulard, T.. CFD prediction of the natural ventilation in a  
720 tunnel-type greenhouse: Influence of wind direction and sensibility to tur-  
721 bulence models. *Proceedings of the International Conference on Sustainable*  
722 *Greenhouse Systems, Vols 1 and 2* 2005;.

723 Santolini, E., Pulvirenti, B., Benni, S., Barbaresi, L., Torreggiani, D., Tassinari,  
724 P.. Numerical study of wind-driven natural ventilation in a greenhouse  
725 with screens. *Computers and Electronics in Agriculture* 2018;149:41–53.

726 Santolini, E., Pulvirenti, B., Torreggiani, D., Tassinari, P.. Novel methodolo-  
727 gies for the characterization of airflow properties of shading screens by means  
728 of wind-tunnel experiments and cfd numerical modeling. *Computers and*  
729 *Electronics in Agriculture* 2019;163. doi:10.1016/j.compag.2019.05.009.

730 Santolini, E., Torreggiani, D., Tassinari, P.. Shading screens characterization  
731 by means of wind tunnel experiments and cfd modeling. 2020. doi:10.1007/  
732 978-3-030-39299-4\_36.

733 Sapounas, A., Hemming, S., De Zwart, H., Campen, J.. Influence of  
734 Insect Nets and Thermal Screens on Climate Conditions of Commercial Scale  
735 Greenhouses: a Cfd Approach. *XVIIth World Congress of the International*  
736 *Commission of Agricultural and Biosystems Engineering (CIGR)* 2010;:1–11.

- 737 Valera, D.L., Álvarez, A.J., Molina, F.D.. Aerodynamic analysis of several  
738 insect-proof screens used in greenhouses. Spanish Journal of Agricultural  
739 Research 2006;4:273–279.
- 740 Valera, D.L., Molina, F.D., Álvarez, A.J., López, J.A., Terrés-Nicoli, J.M.,  
741 Madueño, A.. Contribution to characterisation of insect-proof screens: Ex-  
742 perimental measurements in wind tunnel and cfd simulation. Acta Horti-  
743 culturae 2005;691:441–448.
- 744 Vanderkooy, J.. AES: Journal of the Audio Engineering Society  
745 1994;42(4):219–231.
- 746 Yakhot, V., Orszag, S.A., Thangam, S., Gatski, T.B., Speziale, C.G..  
747 Development of turbulence models for shear flows by a double expan-  
748 sion technique. Physics of Fluids A: Fluid Dynamics 1992;4(7):1510–1520.  
749 doi:10.1063/1.858424.